Acta Materialia 285 (2025) 120660

Contents lists available at ScienceDirect

Acta Materialia

journal homepage: www.elsevier.com/locate/actamat

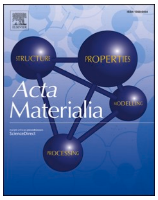

A novel two-step grain boundary diffusion process using TaF_5 and $Pr_{70}Cu_{15}Al_{10}Ga_5$ for realizing high-coercivity in Nd-Fe-B-sintered magnets without use of heavy rare-earth

Seol-mi Lee [a,b], Ganghwi Kim [c], Ki-Suk Lee [c], Sumin Kim [a], Tae-Hoon Kim [a,*], Sang-hyub Lee [d], Dong-Hwan Kim [d], Wooyoung Lee [b,*], Jung-Goo Lee [a]

[a] *Department of Magnetic Materials, Korea Institute of Materials Science, Changwon 51508, Republic of Korea*
[b] *Department of Materials Science and Engineering, Yonsei University, Seoul 03722, Republic of Korea*
[c] *School of Materials Science and Engineering, Ulsan National Institute of Science and Technology, Ulsan 44919, Republic of Korea*
[d] *R&D Center, Star Group Ind. Co., Ltd., Daegu 42714, Republic of Korea*

ARTICLE INFO

Keywords:
Nd-Fe-B-sintered magnets
Heavy rare-earth-free
Grain boundary diffusion process
Chemically induced liquid film migration
Intergranular precipitates

ABSTRACT

To achieve high-coercivity in Nd-Fe-B-sintered magnets without relying on the use of heavy rare-earth (HRE), developing an HRE-free grain-boundary-diffusion-process (GBDP) using the light rare-earth, Pr, is highly desired. The key factor for achieving high-coercivity *via* Pr-GBDP is to increase the Pr-concentration of Pr-rich shell by reducing its thickness, and this can be realized by inhibiting the chemically induced liquid film migration (CILFM) that occurs to form the shell. Herein, for the first time, we report achievement of high-coercivity of 2.35 T without using HRE by developing CILFM-inhibited two-step GBDP that uses TaF_5 to form a intergranular precipitate (PPT) and $Pr_{70}Cu_{15}Al_{10}Ga_5$ to form a Pr-rich shell in the 1st- and 2nd-steps, respectively. Due to the formation of hexagonal-TaB_2 intergranular PPT during the 1st-GBDP, the CILFM is inhibited during the 2nd-GBDP, thereby reducing the grain size and forming the thinner shell with higher Pr-concentration in the magnets. As a result, the μ_0H_c of two-step GBDP magnets (2.35 T) is considerably higher than that of magnets GBD-treated with $Pr_{70}Cu_{15}Al_{10}Ga_5$ alone (1.85 T). A micromagnetic simulation shows that the nucleation field at the interface between the 2–14–1 grain and Nd-rich phase in two-step GBDP magnets increases by such a thinner and higher Pr-concentration shell. Furthermore, due to the CILFM inhibition, the number of Pr atoms consumed for the shell formation near the magnet surface reduces in the two-step GBDP magnets, resulting in an increased GBD-depth of Pr, and this is another contributor for realizing a high-coercivity in magnets *via* the HRE-free two-step GBDP.

1. Introduction

Nd-Fe-B sintered magnets have become an indispensable material for the traction motor of electric or hybrid electric vehicle because their coercivity (μ_0H_c), remanence (μ_0M_r), and maximum energy product [$(BH)_{max}$], critical factors for determining the efficiency of motor, are superior to those of other hard magnetic materials [1,2]. For the traction motor to operate stably at its operation temperature (~200 °C), the μ_0H_c of Nd-Fe-B magnets at room temperature is required to be above 2.5 T [3]. To meet this requirement, heavy rare-earth (HRE) elements, such as Dy or Tb, are alloyed into Nd-Fe-B-sintered magnets [3–6]. The μ_0H_c of $(Nd_{1-x}HRE_x)$-Fe-B magnets undoubtedly improves with increasing x because the anisotropy field, μ_0H_a, of the $Nd_2Fe_{14}B$ (2–14–1) main phase increases by substitution of HRE with Nd [3–6]. However, this leads to a significant reduction in the μ_0M_r and $(BH)_{max}$ of magnets owing to the anti-ferromagnetic coupling between Fe and HRE atoms in the 2–14–1 phase [3–6]. Moreover, the HRE addition deteriorates the cost competitiveness of magnets because of the scarcity of HRE resources [3–8]. To address the limitation of using HREs in high-μ_0H_c magnet fabrication, Nakamura and Hirota et al. proposed the grain boundary diffusion process (GBDP) using the HRE [9,10]. The HRE-GBDP significantly increases the μ_0H_c of Nd-Fe-B sintered magnets with minimal HRE usage because the grain boundary diffused HRE atoms dissolve only into the surface region of 2–14–1 grains, forming a high-μ_0H_a (Nd,

---

* Corresponding authors.
E-mail addresses: chopkr@kims.re.kr (T.-H. Kim), wooyoung@yonsei.ac.kr (W. Lee).

https://doi.org/10.1016/j.actamat.2024.120660
Received 16 September 2024; Received in revised form 15 November 2024; Accepted 14 December 2024

HRE)$_2$Fe$_{14}$B shell (HRE-rich shell) that can suppress the reverse domain nucleation at the interface between the 2–14–1 grain and Nd-rich grain boundary phase (GBP) [6,9–14]. Since the HRE atoms that anti-ferromagnetically couple with Fe are localized in the HRE-rich shell region, the μ_0M_r and $(BH)_{max}$ of the HRE-GBDP magnets are also much higher than those of the HRE-alloyed magnets [6,9–14]. However, the problem of HRE resource shortage has become more serious recently, and this has attracted great interest into realizing high-μ_0H_c in Nd-Fe-B sintered magnets *via* HRE-free GBDP [15–17].

The light rare-earth (LRE) element Pr seems to be the most suitable diffusion source for the HRE-free GBDP because the Pr-GBDP also forms a Pr-rich (Nd, Pr)$_2$Fe$_{14}$B shell with a higher μ_0H_a compared with that of $Nd_2Fe_{14}B$ (μ_0H_a of $Pr_2Fe_{14}B$: ~8.5 T, μ_0H_a of $Nd_2Fe_{14}B$: ~7.0 T) [15–38]. In addition, because of the slightly less negative formation enthalpy of $Pr_2Fe_{14}B$ (–0.04 eV/atoms) than that of $Nd_2Fe_{14}B$ (–0.06 eV/atoms) [10], some of the grain boundary diffused Pr atoms dissolve into the Nd-rich GBP rather than the 2–14–1 grain, thereby increasing the thickness and Pr concentration of the GBP after the Pr-GBDP [15–38]. As a result, the exchange coupling between neighboring 2–14–1 grains is weakened by the Pr-dissolved thick GBP, and the nucleation field at the 2–14–1//GBP interface is increased by the high-μ_0H_a Pr-rich shell, which leads to improvement in μ_0H_c of magnets after the Pr-GBDP [15–38]. However, the μ_0H_c gain by Pr-GBDP is only 0.2−0.3 T [18–20], which is insufficient to realize a high-μ_0H_c above 2.5 T that can be achieved in HRE-free magnets by the HRE-GBDP [39,40]. In addition, due to an increase in the volume fraction of the non-ferromagnetic Nd-rich GBP, μ_0M_r, which is defined as $f\bullet(1\text{-}V_{\text{non-ferro}})\bullet\mu_0M_s$, ($f$: [001]-texture, $V_{\text{non-ferro}}$: volume fraction of non-ferromagnetic phases), noticeably decreases after the Pr-GBDP [4]. Thus, in the case of the Pr-GBDP, μ_0M_r of base magnets is required to be high to compensate for μ_0M_r reduction after the GBDP. Considering that μ_0H_c of commercial HRE-free magnets with high-μ_0M_r above 1.4 T is in the range of 1.3−1.8 T [41], the μ_0H_c gain by the Pr-GBDP should be at least 0.7−1.2 T to obtain a μ_0H_c of 2.5 T in HRE-free magnets with the Pr-GBDP. To achieve this, considerable effort has been made to increase the GBD-depth of Pr and modify the microstructure of the Nd-rich GBP by alloying the Pr with non-ferromagnetic metals, such as Al, Cu, Ga *etc.,* which can lower the melting point of Pr [15–17,21–38,42–44]; however, the μ_0H_c gain achieved with the Pr-alloy-GBDP has so far been ~0.6 T [15–17,21–38], which is still not large enough to replace the HRE-GBDP. To breakthrough such a limitation in μ_0H_c of Pr-GBDP magnets, a new guide for developing a highly efficient Pr-GBDP should be provided.

A recent report by Kim et al. provides a novel insight into increasing both the GBD-depth of Pr and Pr-concentration of the Pr-rich shell, which are critical factors for achieving a high-μ_0H_c with the Pr-GBDP [14]. They found that shell formation induces undesirable grain growth during the GBDP because a unique grain boundary migration phenomenon, termed chemically induced liquid film migration (CILFM), is dominantly involved in the shell formation [14]. By the CILFM, Nd-rich GBP migrates while consuming the GBD source, leaving the shell behind [14,45,46]. As a result, the size of 2–14–1 grains increases in proportion to the thickness of the shell formed during the GBDP [14,45, 46]. For this reason, the 2–14–1 grains observed in the thick-shell-forming region (*e.g.*, near surface region of GBDP magnets) are always larger than those observed in the thin-shell-forming region (*e.g.*, central region of GBDP magnets) [14,24]. Based on the results from a detailed microstructure analytical works on the GBDP magnets, the CILFM can be defined as i) GBD source consuming and ii) grain coarsening phenomenon [14,40]. This directly indicates that if the CILFM is hindered during the Pr-GBDP, the GBD-depth of Pr can be increased and undesirable grain growth occurred during the Pr-GBDP can be suppressed, thereby improving the μ_0H_c of Pr-GBDP magnets further. An important point to note here is that inhibiting the CILFM can also reduce the thickness of the Pr-rich shell, which could lead to an increase in the Pr-concentration of the Pr-rich shell as reported by Kim et al. and Oikawa et al. [14,47]. According to a previous micromagnetic simulation [47], the critical determinant for μ_0H_c of GBDP magnets is not the thickness of the shell but the μ_0H_a of shell [47]. This indicates that controlling the thickness and Pr-concentration of the Pr-rich shell to be thinner and higher, respectively, is favorable for achieving a higher μ_0H_c with the Pr-GBDP, and this microstructurally optimized shell can be obtained by inhibiting CILFM. Thus, to breakthrough the limit of the μ_0H_c gain by the Pr-GBDP, a CILFM-inhibited GBDP should be developed.

Forming the intergranular precipitate (PPT) in the magnets prior to the Pr-GBDP is one of the effective ways to develop the CILFM-inhibited Pr-GBDP. According to the previous investigations [54–61], the intergranular PPT can be easily formed in the Nd-Fe-B magnets by alloying refractory metals (RM), such as Ta, Ti, Zr, Nb, Mo, W, *etc* [48–53]. However, in this case, an RM-containing PPT is formed not only along the Nd-rich GBP but also within the 2–14–1 grains, and such an intragranular PPT acts as a nucleation site of the reverse domain [51,53]. In addition, in the RM-alloyed magnets, the PPT is formed at center region of the magnet as well as surface region [51,53]. Since CILFM occurs more actively in the area closer to the magnet surface, such a PPT formed at the center part of magnets is not necessary to inhibit the CILFM effectively. From this viewpoint, the utilization of RM as a GBD source is crucial for developing a CILFM-inhibited GBDP, *i.e.*, two-step GBDP consisting of the 1st-GBDP using RM and the 2nd-GBDP using Pr can be a novel method for obtaining a high-μ_0H_c in Nd-Fe-B magnets by inhibiting the CILFM during the Pr-GBDP. Considering that the GBD coefficient (D_b) of the GBD source increases as its melting temperature decreases, both the melting point of RM for 1st-GBDP and Pr for 2nd-GBDP should be reduced. It has been reported that RM-fluorides, such as TaF_5 (T_m: 96.8 °C), NbF_5 (T_m: 72 °C), and MoF_5 (T_m: 45.7 °C) have a very low melting temperature of less than 100 °C [54,55]. In addition, it is well known that the melting point of Pr is effectively reduced by alloying with non-ferromagnetic Al, Cu, or Ga as described above [15–17,21–38,42–44]. Thus, in this work, we developed a CILFM-inhibited two-step GBDP consisting of TaF_5GBDP (1st-GBDP) for forming a Ta-containing intergranular PPT and the $Pr_{70}Cu_{15}Al_{10}Ga_5$-GBDP (2nd-GBDP) for forming Pr-rich shell with a high-μ_0H_a and modifying microstructure of the Nd-rich GBP. By the two-step GBDP developed in this work, for the first time, the μ_0H_c gain of 0.91 T [1.44 T (annealed base magnets) → 2.35 T (two-step GBDP magnets)] was achieved without using the HRE. To explain the microstructural superiority of the two-step GBDP magnets in terms of the CILFM inhibition, the grain size, GBD-depth of Pr, and thickness/Pr-concentration of the Pr-rich shell in the two-step GBDP magnets were intensively investigated in comparison with those in the magnets produced *via* GBDP with $Pr_{70}Cu_{15}Al_{10}Ga_5$ alone. We also conducted a micromagnetic simulation to explain how such a large μ_0H_c gain could be achieved by the two-step GBDP. Based on the microstructure analysis and micromagnetic simulation results, a guide for developing a high-efficiency HRE-free GBDP to produce high-μ_0H_c Nd-Fe-B magnets is proposed.

2. Experimental

2.1. Preparation and characterization of samples

The as-sintered HRE-free magnets with a nominal composition of $Nd_{10.6}Pr_{3.1}Fe_{79.6}B_{5.4}M_{1.3}$ (at.%) or 23.3Nd−6.7Pr−68.0Fe−0.9B−1.1M (wt.%), where M = Al, Co, Cu, and Ga, were used as base magnets. The dimensions of the base magnets prepared for GBDP were 12.5 mm (a) × 12.5 mm (b) × 3.7 (c, easy-axis) mm. The $Pr_{70}Cu_{15}Al_{10}Ga_5$ (at.%) or 86.3Pr−8.3Cu−2.4Al−3.0Ga (wt.%) alloy powders for the GBDP were fabricated by melt-spinning with a Cu wheel at a speed of approximately 26 m/s. Hereafter, the Pr−Cu−Al−Ga alloy is denoted as PCAG. To diffuse TaF_5 into the base magnets prior to the PCAG-GBDP, 1.0 wt.% of TaF_5 with a melting point of 96.8 °C was uniformly coated on the a–b planes of the base magnets. The low melting point of TaF_5 allowed it to easily adhere to the magnet surfaces by heating at 90 °C in an oven for

Table 1
Characteristics of Pr-rich shells for micromagnetic simulation.

Thickness (cells)	Volumetric fraction (%)	Pr-substitution rate (%)	M_s (10^6 A/m)	K_{u1} (10^6 J/m^3)
2	13.56	86.62	1.2467	5.3662
4	25.89	62.04	1.2565	5.1204
6	37.06	53.89	1.2598	5.0389
8	47.10	49.86	1.2614	4.9986
10	56.05	47.49	1.2623	4.9749

10 min. Then, the TaF_5-coated magnets were heat-treated at 900 °C for 1 h. for the GBD of low-melting TaF_5 into the base magnets (1st-step GBDP). The 8.0 wt.% of PCAG was then coated on the *a–b* planes of TaF_5-GBDP magnets using PVA and ethanol solutions, and the magnets were heat-treated at 970 °C for 15 h. for the GBD of PCAG into the TaF_5-GBDP magnets (2nd-step GBDP). Subsequently, the samples were annealed at 550 °C for 2 h. Hereafter, the two-step GBDP magnets are denoted as T-PCAG magnets. For comparison, magnets GBD treated with PCAG alone (PCAG magnets) were also prepared.

The magnetic properties of the samples were measured using a BH-hysteresis loop tracer (PERMAGRAPH C300, MAGNET-PHYSIK). To ensure that the melt-spun ribbons were in a suitable condition for the GBDP, their melting temperature was evaluated using a differential scanning calorimeter (DSC, Labsys^{TM}TG, SETARAM Instrumentation) under an Ar atmosphere at a heating rate of 10 °C/min. The melting point of PCAG was determined to be approximately 710 °C, which was considerably lower than that of pure Pr (T_m: ~930 °C). An overall microstructure observation was performed using field emission scanning electron microscopy (FE-SEM) and an electron probe microanalyzer (FE-EPMA, JXA8530F, JEOL). The structure and chemistry of the intergranular PPT, Pr-rich shell, and Nd-rich GBPs were examined using scanning transmission electron microscopy (FE-STEM, Talos F200X, Thermo Fisher Scientific) combined with an energy-dispersive X-ray spectrometry (EDS) and a selected area diffraction pattern (SADP). The STEM specimens were prepared using lift-out and Ga ion-thinning methods using a focused ion beam (FIB, Scios2, Thermo Fisher Scientific).

2.2. *Micromagnetic simulation*

To elucidate the relationship between the microstructure and μ_0H_c of the magnets, micromagnetic simulations were performed. The simulation calculates the variation of the magnetization structure by solving the precession-less Landau–Lifshitz–Gilbert (LLG) equation based on the finite difference method (FDM) [56,57], using MuMax3 [58]. The smallest unit of the system was a 2.0 nm × 2.0 nm × 2.0 nm cubic cell, and the system was composed of 256 × 256 × 256 cells. The entire system was divided into 64 grains with 120 nm average diameter based on Voronoi tessellation, and each grain was separated by a GBP with the thickness of 5 nm. The thin parts of the grain near the GBP were separately designated as a different region from the inner grain to construct the core-shell structure. The shell thickness varied from 5.0 nm to 25.0 nm. The entire system was uniformly magnetized in the +z-direction, and an external magnetic field was applied in the −z-direction from $\mu_0H_z = -1.0$ T to −3.0 T, with an intervals of 0.01 T.

The chemical compositions of the core and shell were determined based on the compositions estimated by a TEM-EDS elemental map. The core was fixed as $(Nd_{0.65}Pr_{0.35})_2Fe_{14}B$ for all simulation cases. The composition of the shell was set to two different cases. The first case was adjusted to emulate the effect of CILFM inhibition on the thickness and Pr-concentration of the shell. The average Pr-substitution rate of the entire system was fixed at 42 %, thus the Pr-concentration of the shell was inversely proportional to the shell thickness. The detailed compositions of the shells used in the simulations are listed in Table 1. The volumetric fraction of the shell was 13.56 % when the shell thickness was 5 nm, hence Pr-substitution rate of shell was 86.62 %. As the shell thickened, the volumetric fraction of the shell increased, and the substitution rate of shell decreased to 47.49 % when the shell thickness was 25 nm. The second case ignored the effect of CILFM, *i.e.*, the Pr-composition of the shell was independent of the thickness. The Pr-substitution rate was fixed at 86.62%, which was the same as the 2 nm-thickness shell of the first case.

For $Nd_2Fe_{14}B$, the saturation magnetization, M_s, = 1281.2 × 10^3 A/m, uniaxial anisotropy constant, K_{u1}, = 4500 × 10^3 J/m^3, and for $Pr_2Fe_{14}B$, the $M_s = 1241.4 \times 10^3$ A/m, and $K_{u1} = 5500 \times 10^3$ J/m^3 [4]. The exchange stiffnesses (A_{ex}) of both the core and shell were 8.0 × 10^{-12} J/m [59]. The magnetic properties of the core and shell were estimated by the linear interpolation of the Pr-substitution rate [47]. The parameters of the GBP were $M_s = 397.9 \times 10^3$ A/m, $K_{u1} = 0.0$ J/m^3, and $A_{ex} = 6.0 \times 10^{-12}$ J/m [60,61]. The direction of the easy-axis for each grain was defined by a normalized vector, and its polar angle followed a Gaussian distribution so that the average value of the *z*-component of the easy-axis vector was 0.8.

3. Results and discussion

Fig. 1(a) shows the demagnetization curves for as-sintered HRE-free base magnets (grey line), PCAG magnets (blue line, one-step GBD treated with $Pr_{70}Cu_{15}Al_{10}Ga_5$), and T-PCAG magnets [red line, two-step GBD treated with TaF_5 (1st-GBD) and $Pr_{70}Cu_{15}Al_{10}Ga_5$ (2nd-GBD)], respectively. The demagnetization curve for optimally annealed base magnets is also displayed as a dark grey line. The μ_0H_c of base magnets was 1.29 T, which increased to 1.44 T by annealing, as shown in Fig. 1

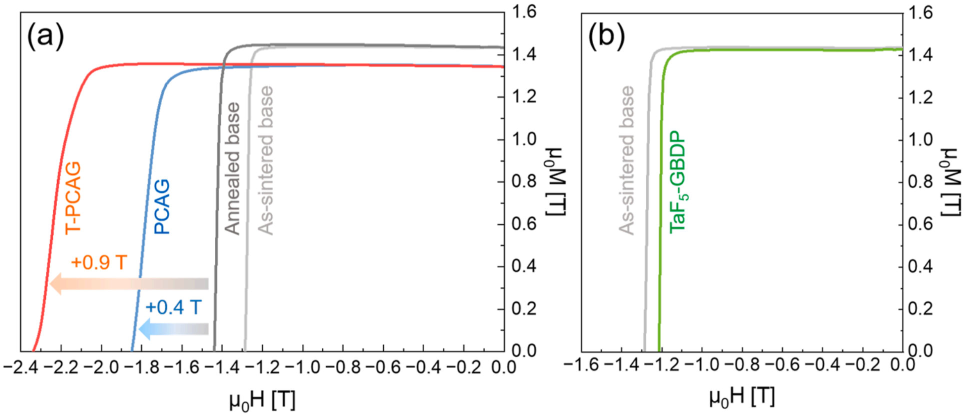

Fig. 1. (a) Demagnetization curves for as-sintered base magnets (grey line), optimally annealed base magnets (dark grey line), PCAG magnets (blue line), and T-PCAG magnets (red line). (b) Effect of GBDP with TaF_5 alone on magnetic properties of as-sintered base magnets.

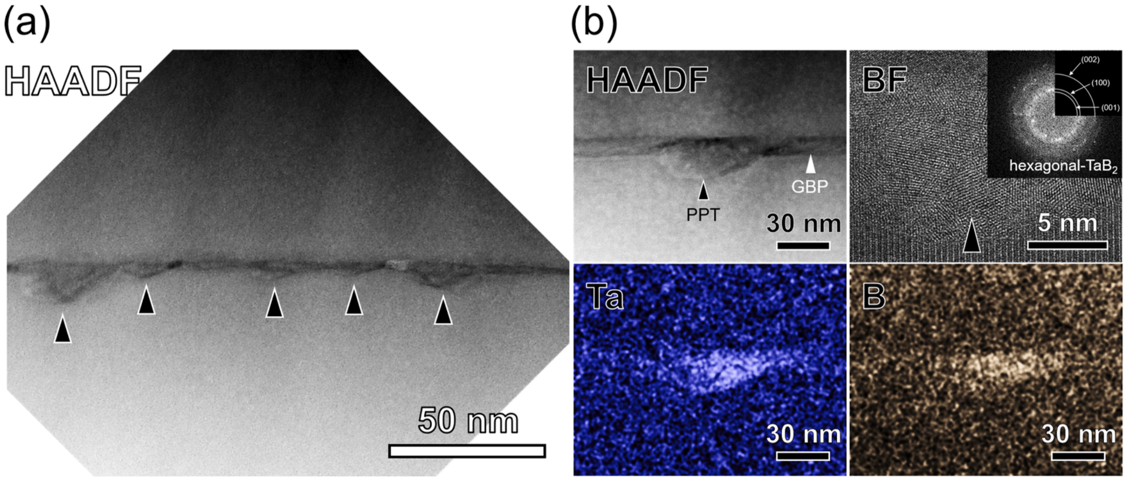

Fig. 2. (a) HAADF-STEM image of Nd-rich GBP located at a ~100 μm depth of TaF$_5$-GBDP magnets. The formation of intergranular PPTs with sizes of 10–30 nm is clearly observed as indicated by triangles. (b) HAADF-STEM image and EDS elemental maps for Ta and B of intergranular PPT shown in (a). The high-resolution BF-TEM image and its fast Fourier transformed image are also shown. Based on the results, the intergranular PPTs formed in TaF$_5$-GBDP magnets is clearly identified as polycrystalline hexagonal-TaB$_2$.

(a). The μ_0M_r of base magnets (1.43 T) remained unchanged after annealing. After undergoing the PCAG-GBDP, the μ_0H_c of the magnets increased to 1.85 T, while the μ_0M_r decreased to 1.35 T. The μ_0H_c gain (0.41 T) and μ_0M_r loss (0.08 T) by the PCAG-GBDP shown in Fig. 1(a) are comparable to those reported elsewhere [15–38]. It should be noted that the μ_0H_c of magnets dramatically increased to 2.35 T by the two-step T-PCAG-GBDP, resulting in a very large μ_0H_c gain of 0.91 T without using HRE, as shown in Fig. 1(a). According to previous results [15–38], the μ_0H_c gain achievable with the Pr-GBDP is limited to ~0.6 T, thus there has been no options other than use of expensive HRE-GBDP to obtain such a large μ_0H_c gain of 0.91 T, as shown in Fig. 1(a). This indicates that the two-step T-PCAG-GBDP developed in this work is a promising method that can replace the HRE-GBDP for producing high-μ_0H_c Nd-Fe-B sintered magnets. Interestingly, as shown in Fig. 1(b), the μ_0H_c of magnets slightly decreased by the TaF$_5$-GBDP alone. In order to clarify the role of the 1st-GBDP with TaF$_5$, which appeared to be a core step of the two-step T-PCAG-GBDP, the microstructure observation of TaF$_5$-GBDP magnets was carried out first, as shown in Fig. 2. Fig. 2(a) shows a high-angle annular dark-field (HAADF)-STEM image of the Nd-rich GBP located at a depth of ~100 μm of the TaF$_5$-GBDP magnets. It was clearly seen that very fine PPTs with sizes of 10–30 nm were formed along the Nd-rich GBP as indicated by the triangles in Fig. 2(a). Fig. 2(b) shows the HAADF-STEM, bright-field (BF)-TEM, fast Fourier transformed (FFT), and EDS mapping images taken from the intergranular PPT shown in Fig. 2(a). The PPT was clearly identified as the polycrystalline hexagonal-TaB$_2$ phase. According to the previous reports [51,53], such an intergranular PPT in the magnets could act as a nucleation site of the reverse domain [51,53], which implies that the slight reduction in the μ_0H_c of magnets after the TaF$_5$-GBDP shown in Fig. 1(b) is attributed to the formation of a hexagonal-TaB$_2$ intergranular PPT.

Now, the question is why the μ_0H_c of TaF$_5$-GBDP magnets containing a TaB$_2$ PPT improved more significantly with the PCAG-GBDP compared to as-sintered magnets containing no PPT, as shown in Fig. 1(a). To answer the question, the microstructure of T-PCAG and PCAG magnets were comparatively studied, specifically focusing on the influence of the TaB$_2$ intergranular PPT on the thickness and chemistry of the Pr-rich shell formed by the chemically induced liquid film migration (CILFM) [14], as follows.

3.1. Microstructural differences between T-PCAG and PCAG magnets as a function of magnet depth

Fig. 3(a) and (b) show the BSE-SEM images and EPMA elemental

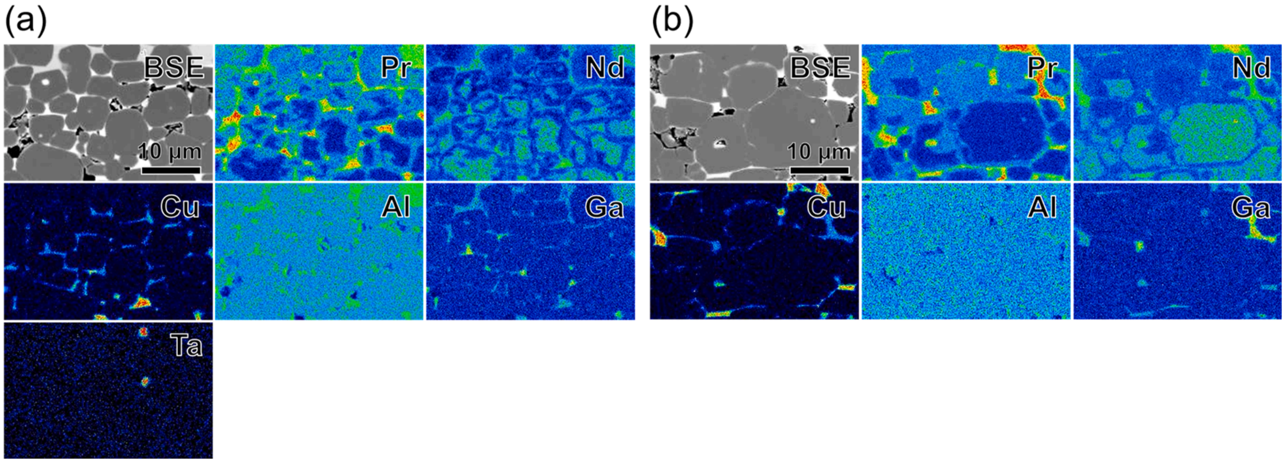

Fig. 3. BSE-SEM and EPMA elemental mapping images taken at a ~20 μm depth of (a) T-PCAG and (b) PCAG magnets. The GBD direction of the PCAG sources is from top to bottom of images. The uniform distribution of Pr within 2–14–1 grain observed in the top of the images is due to the lattice diffusion of Pr that commonly occurs on the magnet surface during the GBDP. The black contrast in the BSE images correspond to the area damaged by the mechanical polishing.

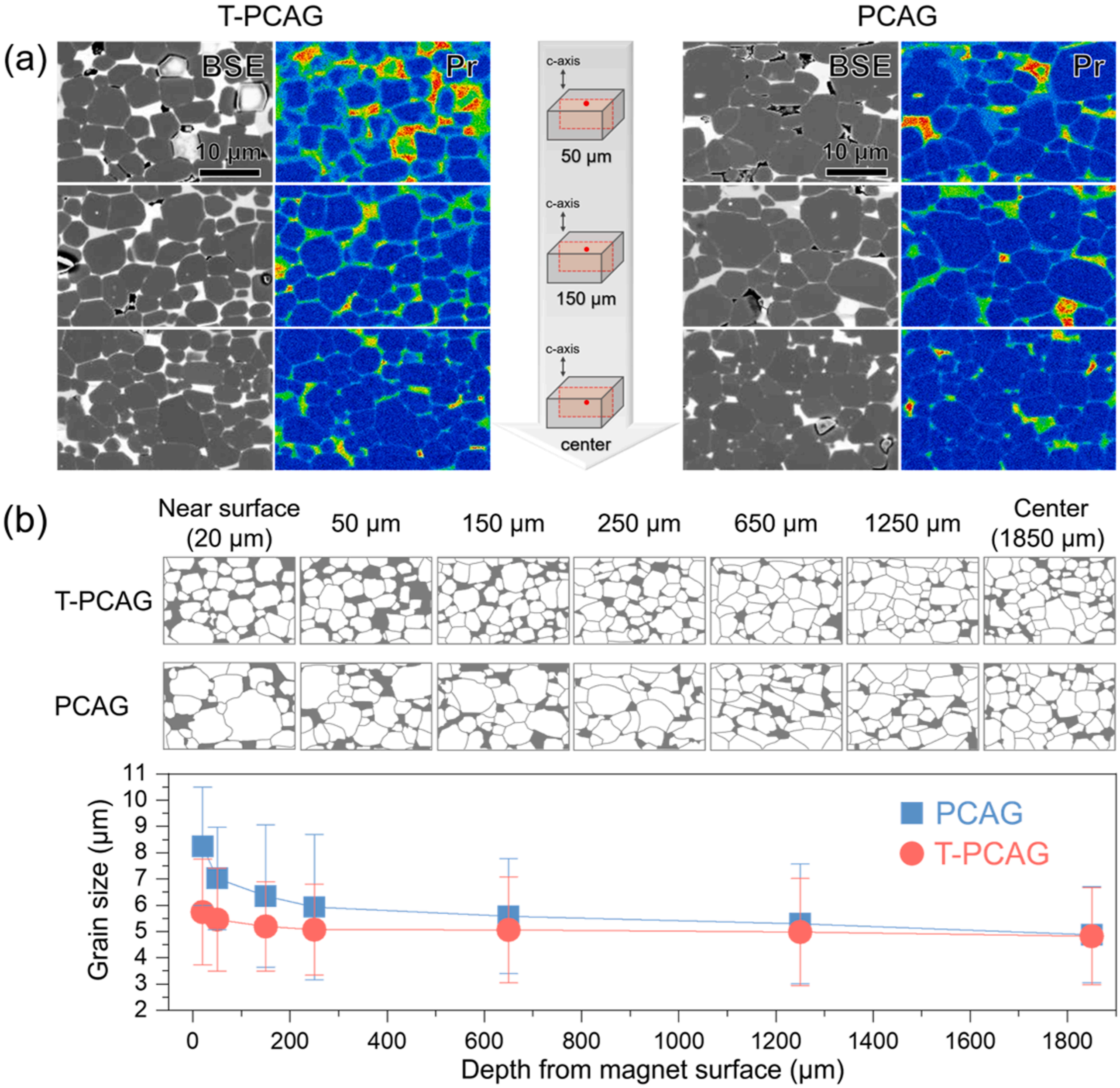

Fig. 4. (a) BSE images and EPMA maps for Pr of T-PCAG and PCAG magnets taken at ~50 μm, ~150 μm, and center (~1850 μm) of samples. The GBD direction of the PCAG source is parallel to the c-axis of samples, which is indicated by arrows in the schematic illustration in the middle of panel (a). (b) Schematic illustration tracing Nd-rich GBP and measured grain size obtained from BSE images taken at various depths of samples.

maps taken near the surface (~20 μm depth) of T-PCAG and PCAG magnets, respectively. Grey and bright contrasts in the BSE images correspond to the 2–14–1 grain and Nd-rich GBP, respectively. As shown in the BSE images and Pr maps in Fig. 3(a) and (b), the Pr-enrichment in the outer region of the 2–14–1 grain (*i.e.*, formation of Pr-rich shell) was clearly observed in both samples. A uniform distribution of Pr within the 2–14–1 grain was also observed in the upper part of the images, which corresponds to the surface of the samples, because of the lattice diffusion of Pr that commonly occurs on the magnet surface during the GBDP [13, 39,62]. The Cu, Al, and Ga of the PCAG GBDP source, minor elements for reducing the melting point of Pr, were preferentially dissolved into the Nd-rich GBP, as reported elsewhere [15–38,43,44]. In the case of T-PCAG magnets, the formation of very large Ta-containing PPTs with sizes of 0.7−1 μm was observed, as shown in the Ta-map of Fig. 3(a). Such massive PPTs were observed only in the surface region of the magnets, and very fine intergranular PPTs described in Fig. 2 were not detected at the EPMA magnification. As shown in the BSE images of Fig. 3, the morphology of the Nd-rich GBP in the PCAG magnets was curved, while that in the T-PCAG magnets was comparatively flat. The measured average curvature of the GBP in the PCAG magnets is 4.7 times larger than that in the T-PCAG magnets. In addition, the grain size of the PCAG magnets (8.24 ± 2.26 μm) was also much larger than that of the T-PCAG magnets (5.74 ± 2.01 μm). This directly indicates that the CILFM occurred more actively in the PCAG samples than in the T-PCAG samples because one of the strongest pieces of evidence for CILFM is the growth of grain accompanied by GBP bending [14,45,46]. From the viewpoint of grain size and GBP morphology, it is concluded that the CILFM was effectively inhibited in the T-PCAG magnets, and the main factor for their CILFM inhibition was expected to be the formation of the TaB_2 intergranular PPT formed by the 1st-GBD with TaF_5 as shown in Fig. 2 and Ta-map of Fig. 3(a). According to the previous investigation [14], the thickness of the shell becomes thinner if CILFM is inhibited

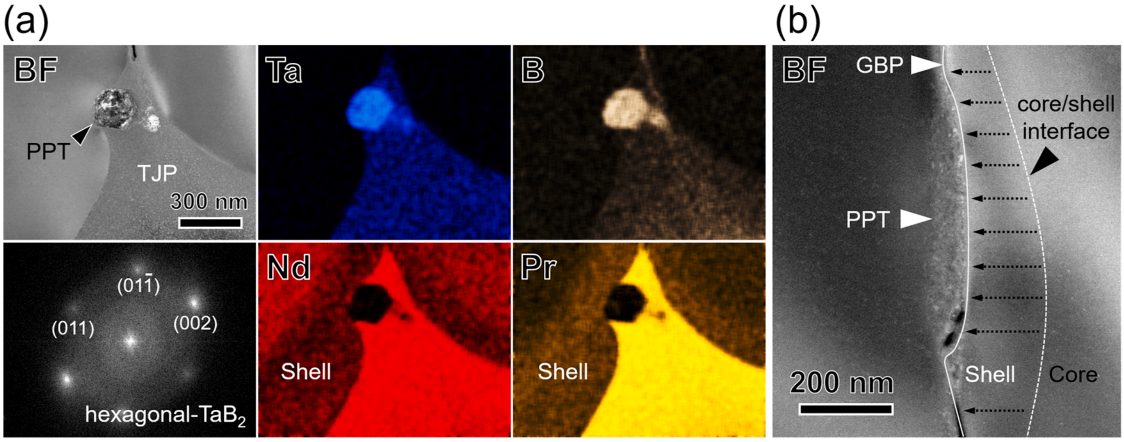

Fig. 5. (a) BF-TEM and EDS mapping images of Nd-rich TJP formed with intergranular PPT taken at a ~150 μm depth of T-PCAG magnets. The FFT image obtained from the PPT is also shown below the BF-TEM image. (b) BF-TEM image of Nd-rich GBP formed with TaB$_2$ PPT. The migration of the GBP and PPT induced by CILFM and Solute drag effect is schematically illustrated on the image.

[14]; however, as shown in Fig. 3(a) and (b), there is no significant difference in the shell thickness of the T-PCAG and PCAG magnets, even if the CILFM seems to be inhibited in the T-PCAG magnets. This discrepancy would be attributed to the slightly less negative formation enthalpy of Pr$_2$Fe$_{14}$B compared with that of Nd$_2$Fe$_{14}$B, which will be discussed in detail later on a microstructural basis.

Fig. 4(a) shows the BSE and Pr mapping images at depths of ~50 μm, ~150 μm, and center (~1850 μm) of the T-PCAG and PCAG magnets. The measured grain sizes and schematic illustrations tracing the GBP, obtained based on the BSE images taken at various depths of the samples, are also shown in Fig. 4(b). As shown in the Pr maps of Fig. 4(a), a gradual decrease in the thickness of the Pr-rich shell as a function of the magnet depth was commonly observed in the T-PCAG and PCAG samples. As shown in Fig. 4(a) and (b), in the case of the PCAG magnets, the size of the 2–14–1 grain was also gradually reduced depending on the magnet depth. It seems that the grain size of the PCAG magnets is a function of the thickness of the Pr-rich shell, and this relationship between the grain size and shell thickness is well consistent with a recent report on the microstructure of Tb-GBDP magnets, in which the CILFM occurs [14]. In contrast to the PCAG magnets, a noticeable change in the grain size depending on the shell thickness (*i.e.*, magnet depth) was not observed in the T-PCAG magnets, as shown in Fig. 4(a) and (b). In addition, compared to the PCAG magnets, much smaller 2–14–1 grain with a comparatively straight Nd-rich GBP was observed in the 20−1250 μm depth region of the T-PCAG magnets. This indicates that the CILFM was effectively inhibited at the entire region of T-PCAG magnets. To confirm the main contributor for the inhibition of CILFM in the T-PCAG magnets, TEM analysis of the Nd-rich triple junction phase (TJP) and GBP regions in the T-PCAG magnets were carried out as shown in Fig. 5. Fig. 5(a) shows the BF-TEM and EDS mapping images of the Nd-rich TJP formed with the intergranular PPT taken at a depth of ~150 μm of the T-PCAG magnets. The FFT image obtained from the PPT is also shown in the 1st-column and 2nd-row of the Fig. 5(a). It can be clearly seen that the ~180 nm sized PPT enriched with Ta and B was formed within the Nd-rich TJP surrounded by the Pr-rich shell. The chemical composition of the PPT was analyzed as Ta$_{33.42}$B$_{66.58}$ (at.%), and its crystal structure was clearly identified as the single crystalline hexagonal-TaB$_2$, as shown in the SADP and EDS maps of Fig. 5(a), which is well agreed with the results shown in Fig. 2(b). The morphology of the Nd-rich GBP formed with the TaB$_2$ PPT is also shown in Fig. 5(b). Note that a thin Pr-rich shell with a thickness of ~160 nm was formed only on the right-side of the GBP, as schematically illustrated in Fig. 5(b). Considering the microstructure of TaF$_5$-GBDP magnets shown in Fig. 2 and the phenomenological feature of CILFM reported in previous investigations [14,45,46], the microstructure shown in Fig. 5(b) indicates that both the GBP and TaB$_2$ PPT initially located at the core/shell interface migrated

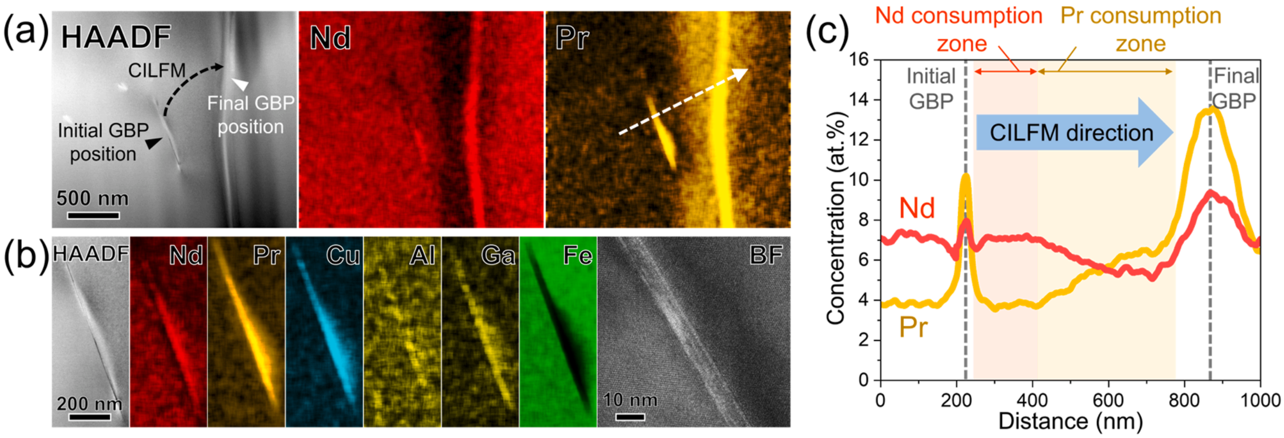

Fig. 6. (a) HAADF-STEM image and EDS elemental maps of Pr-rich shell and Nd-rich GBP in PCAG magnets. The trace of initial GBP located near the core/shell interface and the final migrated GBP is clearly shown as indicated by black and white triangles, respectively. Based on the microstructure shown in panel (a), the direction of the CILFM is predicted as indicated by the black dashed arrow. (b) Microstructure and chemistry of initial GBP trace shown in (a). (c) Line scan profile across initial GBP trace, Pr-rich shell, and final migrated GBP along dashed white arrow in Pr map shown in panel (a). The CILFM zone was found to be divided into Nd consumption and Pr consumption zones.

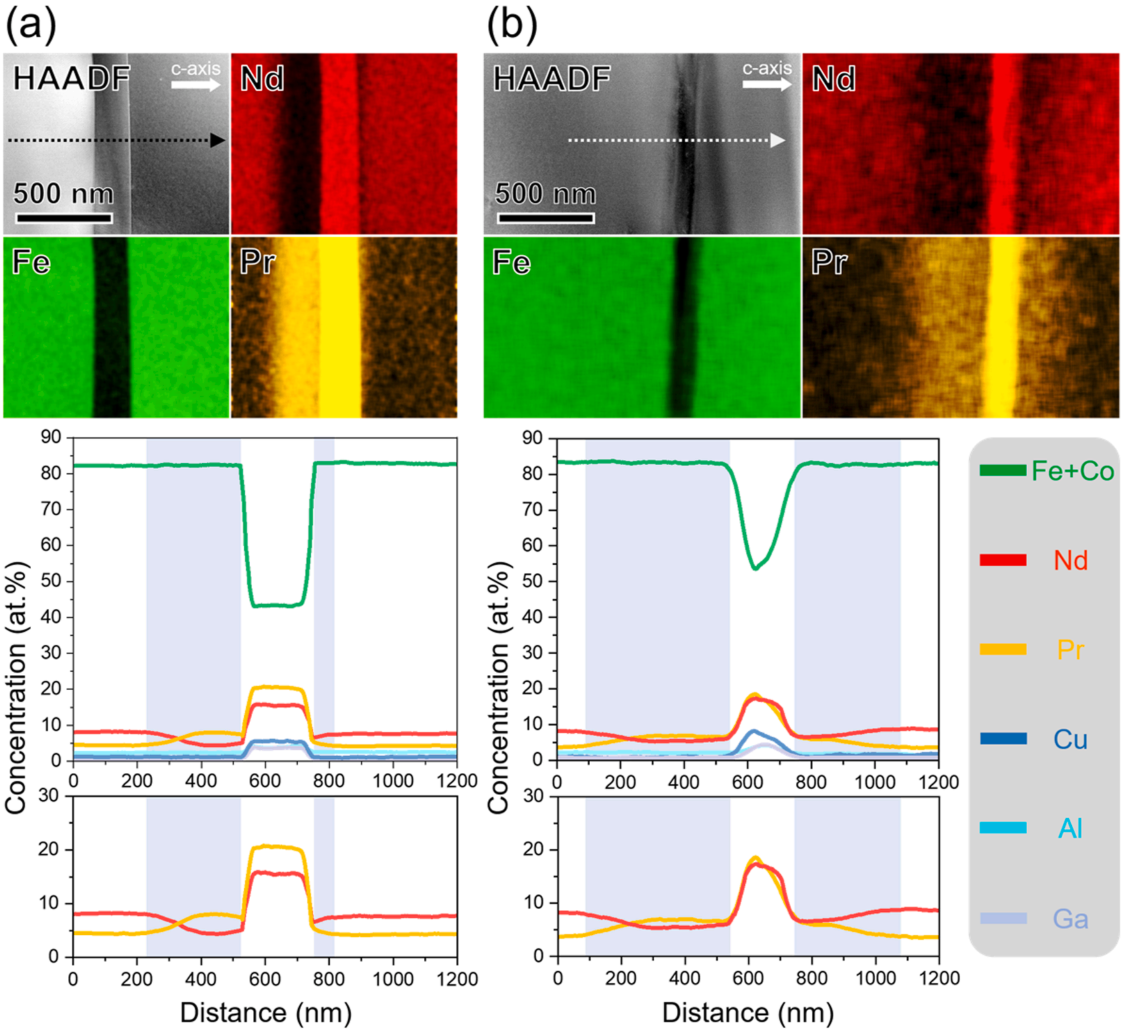

Fig. 7. HAADF-STEM and EDS mapping images of Pr-rich shell and Nd-rich GBP formed at a ~150 μm depth of (a) T-PCAG and (b) PCAG magnets. The c-axis of 2–14–1 main phase is in-plane of the images as indicated by the white arrows. The line scan profiles across the shell and GBP along the dotted arrows in the HAADF-STEM images are also shown in the 2nd-row of the figure. The shell region is highlighted in light blue in the line scan profiles.

together by CILFM and the Solute drag effect [63] from the right to the left side of the figure as indicated by dotted arrows, while leaving the Pr-rich shell behind, but GBP migration was restricted by the drag force of the TaB_2 PPT [63], resulting in the formation of a thin shell [14]. Based on the results shown in Figs. 2–5, it can be concluded that the TaB_2 PPT formed during the 1st-GBDP with TaF_5 is a crucial factor for inhibition of the CILFM occurred to form the Pr-rich shell during the 2nd-GBDP with PCAG.

If the CILFM is inhibited by the TaB_2 PPT as described above, the thickness of the Pr-rich shell should be thinner as observed by Kim et al. [14], because the migration distance of the GBP by CILFM, which is a determinant of the shell thickness, becomes shorten owing to the GBP pinning by the TaB_2 PPT. However, as shown in Figs. 2–4, there was no distinct difference in the shell thickness between the T-PCAG and PCAG samples. The Pr-rich shell of the PCAG magnets was thinner than expected. Fig. 6 provides a clue that can elucidate why the thickness of Pr-rich shell was observed to be thinner in PCAG magnets in which the CILFM occurred actively. Fig. 6(a) shows the HAADF-STEM and EDS mapping images of the Pr-rich shell and Nd-rich GBP in the PCAG magnets. The asymmetric formation of the Pr-rich shell along the GBP enriched with Nd and Pr (white triangle) was clearly observed. Interestingly, another Nd/Pr-enriched phase with a platelet shape was also observed near the core/shell interface as indicated by a black triangle in Fig. 6(a). Fig. 6(b) shows the TEM micrographs and elemental maps of the Nd/Pr-enriched platelet shown in Fig. 6(a). The composition of the platelet was analyzed as $Nd_{8.2}Pr_{10.5}Fe_{68.6}Al_{2.5}Co_{3.6}Cu_{5.4}Ga_{1.2}$ (at.%), and its thickness was measured to be approximately 5 nm. The microstructure and chemistry of the platelet were very similar to those of the GBP commonly observed in the sintered magnets [43,64,65]. According to the previous investigation [14], such trace of the initial Nd-rich GBP that presented before the CILFM occurrence could remain inside the 2–14–1 grain of the GBDP magnets, and its position exactly matches that of the core/shell interface [14]. Thus, the starting position of the CILFM occurrence can be easily predicted by observing the position of the initial GBP trace [14]. Therefore, as schematically illustrated in the HAADF-STEM image of Fig. 6(a), it can be expected that the CILFM started at the position of the Nd/Pr-enriched platelet (*i.e.*, initial GBP position) and it completed at the position of the final migrated GBP, leaving the Pr-rich shell. However, as shown in the Pr map of Fig. 6(a), the position of the initial GBP did not well match that of the core/shell interface. According to the line scan profile taken across the region where the CILFM occurred shown in Fig. 6(c), the CILFM zone can be divided into Nd consumption zone and Pr consumption zone as marked in red and yellow respectively. Considering that the CILFM direction is from the left to right side of Fig. 6(c) as indicated by a blue arrow, it can be expected from Fig. 6(c) that Nd was consumed first to form the shell during the CILFM, and this is probably due to the slightly less negative formation enthalpy of $Pr_2Fe_{14}B$ (–0.04 eV/atoms) compared with that of

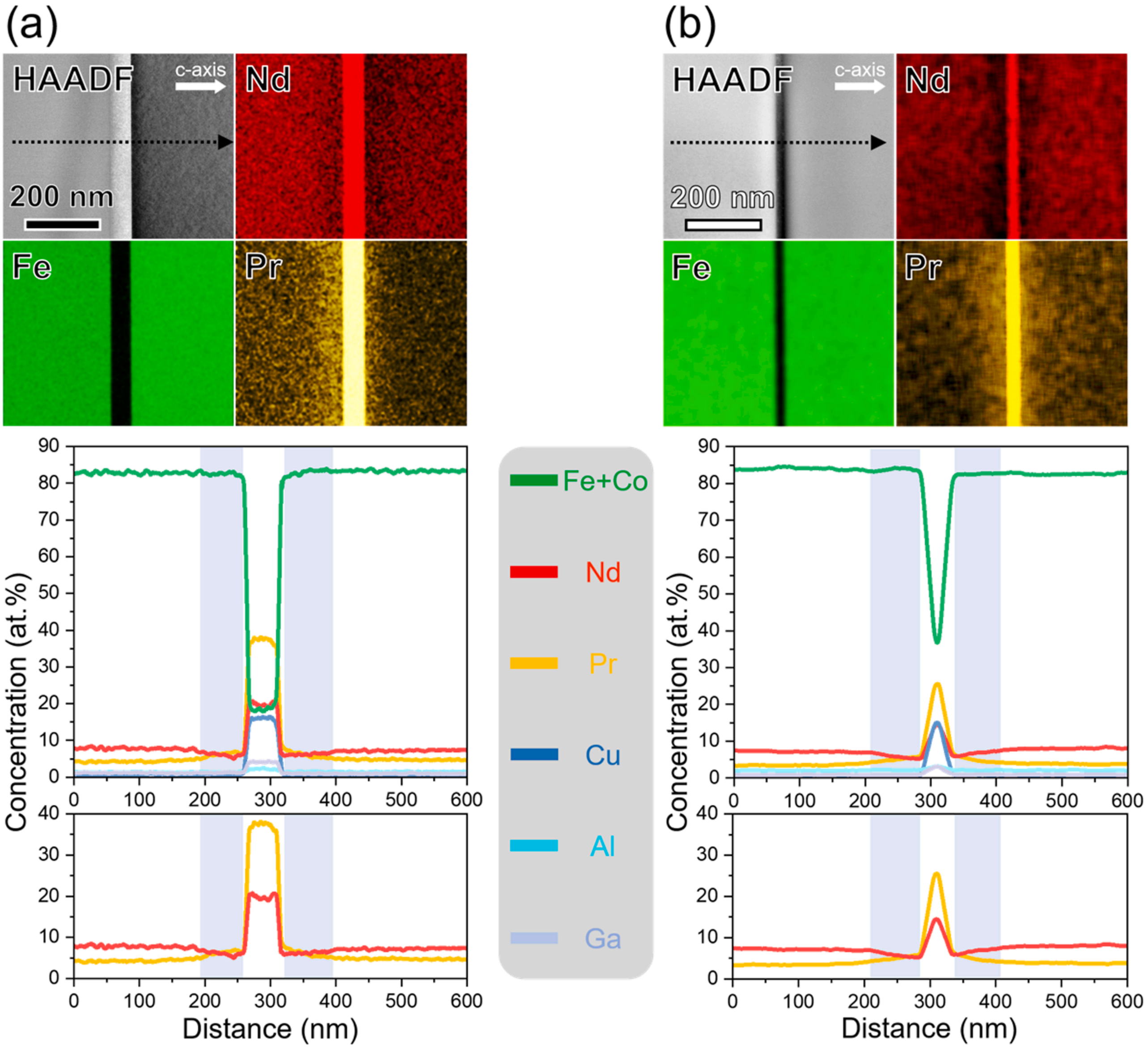

Fig. 8. Microstructure and elemental distribution in Pr-rich shell and Nd-rich GBP formed at a ~1850 μm depth (center) of (a) T-PCAG and (b) PCAG magnets. The line scan profiles shown in the 2nd-row of the figure was obtained along the dotted black arrows in the HAADF-STEM images.

$Nd_2Fe_{14}B$ (–0.06 eV/atoms) [10]. Thereby, in the PCAG magnets, the thickness of the Pr-rich shell was not consistent with the migration distance of the GBP by CILFM as shown in Fig. 6(a) and (c), resulting in the formation of a thinner Pr-rich shell than expected based on the grain size changes shown in Fig. 4(b). This is why a noticeable difference in the thickness of the Pr-rich shell between the T-PCAG and PCAG magnets was not observed, even though grain growth by CILFM occurred more actively in PCAG magnets than in T-PCAG magnets, as shown in Figs. 3 and 4.

When the CILFM is inhibited as described above, the grain boundary diffused Pr could be accumulated into the thin Pr-rich shell or further diffused toward the magnet center, resulting in increasing Pr-concentration of the shell or GBD-depth of Pr. According to the EPMA results shown in Fig. 4(a), the Pr-concentration of the shell and GBD-depth of Pr in the T-PCAG magnets (CILFM-inhibited magnets) seem to be higher and deeper, respectively, than those in the PCAG magnets (CILFM-occurred magnets). These microstructural benefits, which could be a key factor for the large μ_0H_c gain of 0.9 T by the T-PCAG-GBDP shown in Fig. 1, were investigated in detail using TEM as follows.

3.2. Influence of CILFM inhibition on microstructure of Pr-rich shell and GBD-depth of Pr

Fig. 7 shows the HAADF-STEM and EDS mapping images of the Pr-rich shell and Nd-rich GBP formed at a ~150 μm depth of (a) T-PCAG and (b) PCAG magnets. The line scan profiles across the shell and GBP along the dotted arrows in the HAADF-STEM images are also shown in the 2nd-row of the figure. In the case of the PCAG magnets, a slightly curved Nd-rich GBP surrounded by the Pr-rich shell was formed as shown in the HAADF-STEM image and Pr map of Fig. 7(b), and this microstructural character of PCAG magnets is well consistent with the results described in Figs. 3, 4, and 6. The thickness and Pr-concentration of the Pr-rich shell formed on the left side of the GBP were estimated to be ~450 nm and ~5.7 at.%, respectively, and those of the shell formed on the right side of the GBP were estimated to be ~270 nm and ~4.8 at.%, respectively, as shown in Fig. 7(b). For T-PCAG magnets, a straight GBP surrounded by the ~7.9 at.% Pr-containing shell with a ~310 nm thick (left side of GBP) and the ~5.1 at.% Pr-containing shell with a 50 nm thick (right side of GBP), was observed as shown in Fig. 7(a). A slightly thinner Pr-rich shell with a higher Pr-concentration was formed

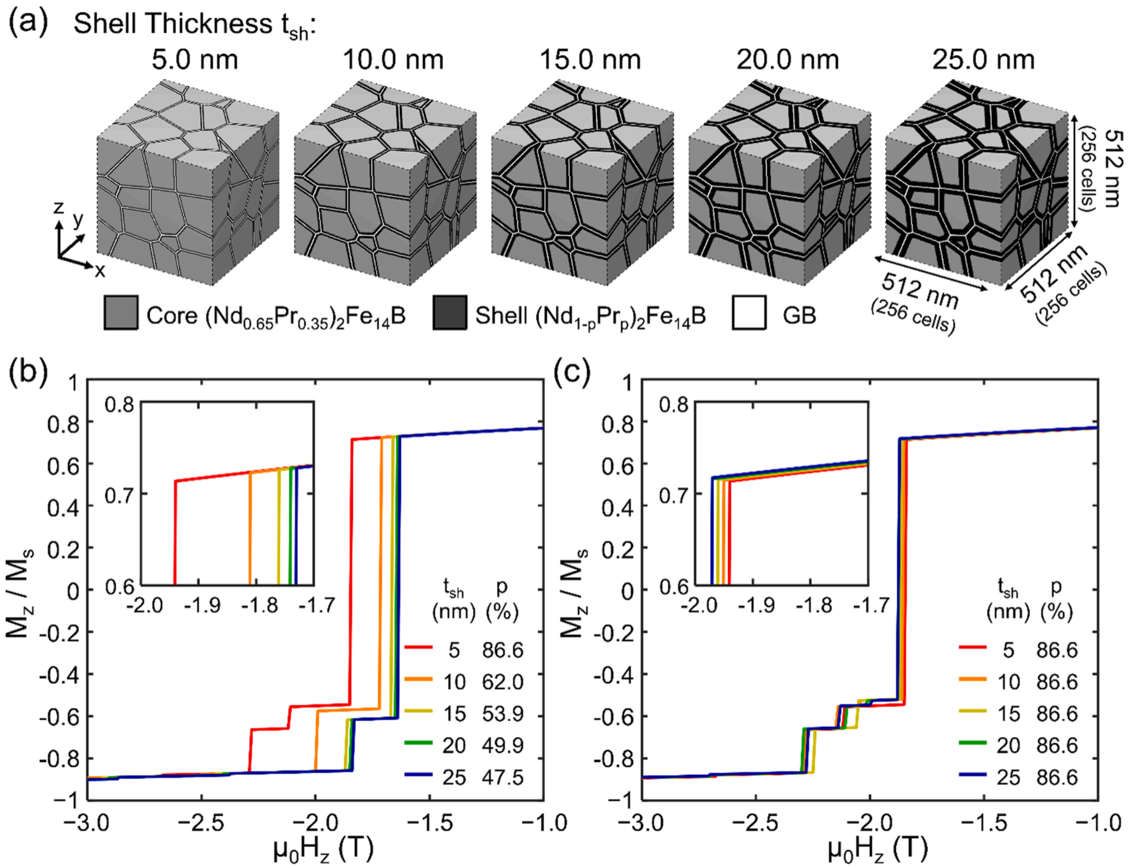

Fig. 9. (a) Structure of core-shell multigrain model. The models are divided into five cases according to the thickness of shell, t_{sh}. The external magnetic field is applied in -*z* direction. (b) and (c) Demagnetization curves for CILFM-inhibited system emulation with (b) various Pr-substitution rate p and (c) fixed p, respectively. The insets in panel (b) and (c) show enlarged demagnetization curves around the nucleation points.

in the T-PCAG magnets compared with that formed in the PCAG magnets. These results demonstrate that CILFM occurred during the Pr-rich shell formation was effectively inhibited in the T-PCAG magnets and this led to an increase in Pr-concentration of the shell. According to the micromagnetic simulation on the Dy-GBDP magnets [47], the most effective way to achieve a high μ_0H_c in Nd-Fe-B magnets by the GBDP is to increase the μ_0H_a of the shell by controlling its Dy-concentration to be higher, and this can be obtained by reducing the shell thickness so that the grain boundary diffused Dy atoms are accumulated and concentrated in the thin shell [47]. Such an ideal shell microstructure in the GBDP magnets was realized by inhibiting the CILFM *via* the two-step T-PCAG-GBDP developed in this work as shown in Fig. 7, thereby obtaining a very large μ_0H_c gain of 0.9 T by the HRE-free GBDP as shown in Fig. 1.

Considering the difference in thicknesses and Pr-concentrations of the shells between the T-PCAG and PCAG samples observed in Fig. 7, the number of Pr atoms involved in the shell formation of the T-PCAG and PCAG magnets is also expected to differ, which could also affect the Pr GBD-depth of the samples, as shown in Fig. 4(a). In order to estimate how many grain boundary diffused Pr atoms dissolved in the shell of the T-PCAG and PCAG magnets, the area under the Pr-concentration curves of the shell region shown in Fig. 7 was integrated. The initially alloyed Pr atoms in the shell were excluded from the integration of the shell region. In the case of PCAG magnets, the area under the Pr-concentration curve of the left side shell region was 1080 and that for the right side shell was 365. Interestingly, in the case of T-PCAG magnets, it was appeared that the area under the Pr-concentration curve of the shell region was much smaller (750 for left side shell and 30 for right side shell), which indicates that less Pr atoms were involved in the Pr-rich shell formation, and thus, more Pr atoms diffused toward the magnet center, resulting in increasing Pr GBD-depth of the T-PCAG magnets, as shown in Fig. 4(a). Such an increased GBD-depth of Pr in the T-PCAG magnets was further clearly observed by TEM observation at the center part of the samples, as shown in Fig. 8. Fig. 8 shows the HAADF-STEM micrographs, EDS elemental maps, and line scan profiles along the dotted lines in the HAADF-STEM images taken at the center part of the (a) T-PCAG and (b) PCAG magnets. The Pr-concentration of the shell in the T-PCAG magnets was higher (~5.6 at.%) than that in the PCAG magnets (~4.4 at.%). Furthermore, the thickness and Pr-concentration of the GBP in the T-PCAG magnets were also thicker and higher than those in the PCAG magnets. Due to an increase in the Pr GBD-depth by the T-PCAG-GBDP, more grain boundary diffused Pr atoms reached the center of the samples, thereby increasing the Pr-concentration of the shell and GBP formed at their center region as shown in Fig. 8, resulting in increasing nucleation field by higher μ_0H_a shell and weakening exchange coupling by the thick and non-ferromagnetic GBP. Therefore, the increased GBD-depth of Pr due to the CILFM inhibition by the T-PCAG-GBDP can be another factor for achieving higher μ_0H_c in the T-PCAG magnets.

According to numerous previous reports on the GBDP magnets, the μ_0H_c enhancement by increasing the GBD-depth of Pr is beyond a doubt [12–40], but the relationship between the μ_0H_c and thickness/Pr-concentration of the shell described in Fig. 7 remains unclear. In order to clarify how the microstructural changes of the Pr-rich shell induced by the CILFM inhibition affected the μ_0H_c of magnets, a micromagnetic simulation was conducted based on the microstructural data obtained from Fig. 7.

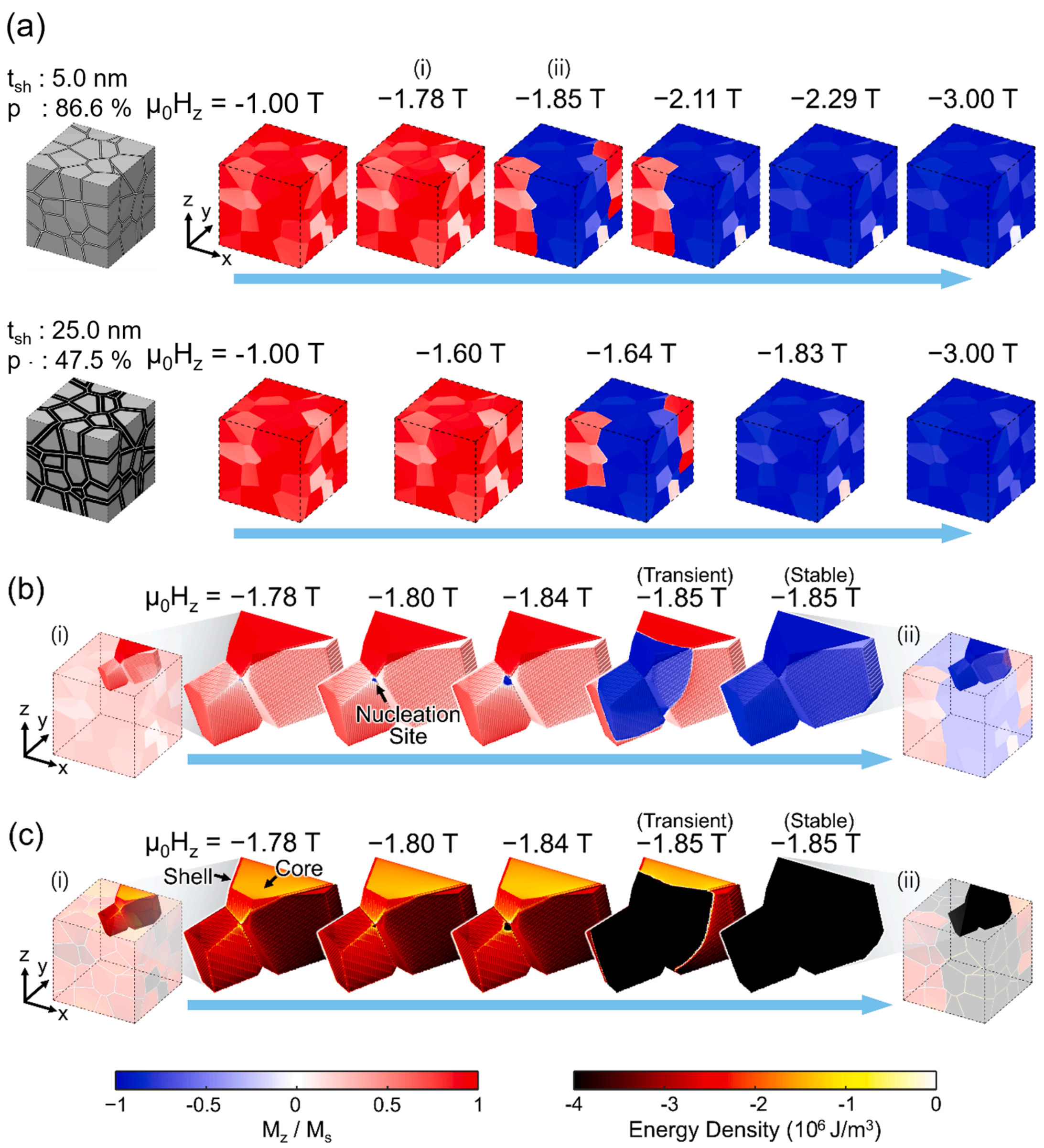

Fig. 10. (a) Demagnetization process for entire CILFM-inhibited system. Upper row: t_{sh} = 5.0 nm, p = 86.6%, Lower row: t_{sh} = 25.0 nm, p = 47.5%. (b) and (c) Variation of magnetization structure and total energy density, respectively, around the nucleation site of CILFM-inhibited system with t_{sh} = 5.0 nm and p = 86.6%. The leftmost and the rightmost images represent the same conditions with the images (i) and (ii) of panel (a), respectively. The grain boundary phase is ignored.

3.3. Microstructure of shell–coercivity relationship

Fig. 9(a) depicts a schematic of the micromagnetic simulation system designed to assess the impact of shell property adjustment by CILFM inhibition. Since the shell is formed by the CILFM mechanism, the Pr-substitution rate of the shell would be lower for a shell thickness (t_{sh}) of 25.0 nm than that for t_{sh} = 5.0 nm. The graph in Fig. 9(b) shows the results of simulation emulating CILFM inhibition. As listed in Table 1, the Pr-substitution rate of the shell (p) decreased from p = 86.6 % with t_{sh} = 5.0 nm to p = 47.5 % with t_{sh} = 25.0 nm. Note that the μ_0H_c of the system decreased from μ_0H_c = 1.84 T with t_{sh} = 5.0 nm to 1.63 T with 25.0 nm. The graph in Fig. 9(c) depicts the results of the simulation at a fixed p of 86.6% and magnetic properties. Contrary to the results shown in Fig. 9(b), only a slight increase in the μ_0H_c from μ_0H_c = 1.84 T with t_{sh} = 5.0 nm to 1.87 T with 25.0 nm was observed as shown in Fig. 9(c). This directly indicates that the μ_0H_c of the GBDP magnets was dominantly determined by the μ_0H_a of the shell not the thickness of the shell as reported by Oikawa et al. [47], and this optimal shell microstructure could be obtained *via* the CILFM inhibition as shown in Fig. 7, thereby obtaining a large μ_0H_c gain after the GBDP, as shown in Fig. 1.

The origin of the high-μ_0H_c of T-PCAG magnets containing thin but high Pr-substitution rate shell was confirmed from the intermediate magnetization structures of the demagnetization process. Fig. 10(a) shows the magnetization reversal process under the applied field from μ_0H_z = −1.0 T to −3.0 T. In the case of t_{sh} = 5.0 nm and p = 86.6 %, the reversed domain was pinned on the GBP area under μ_0H_z = −1.85 T and −2.11 T. For the t_{sh} = 25.0 nm and p = 47.5 %, the domain was pinned under a μ_0H_z = −1.64 T. The domain walls were pinned only on the GBP, not the core-shell boundary; therefore, shell formation did not offer new pinning sites but reinforced existing μ_0H_c enhancement factors. The detailed domain expansion process from state (i) to (ii) in Fig. 10(a) is illustrated in Fig. 10(b). The magnetization structure of three grains near the nucleation site is drawn. Under a μ_0H_z = −1.80 T, the reversed domain was nucleated at a TJP among the grains. The domain slightly

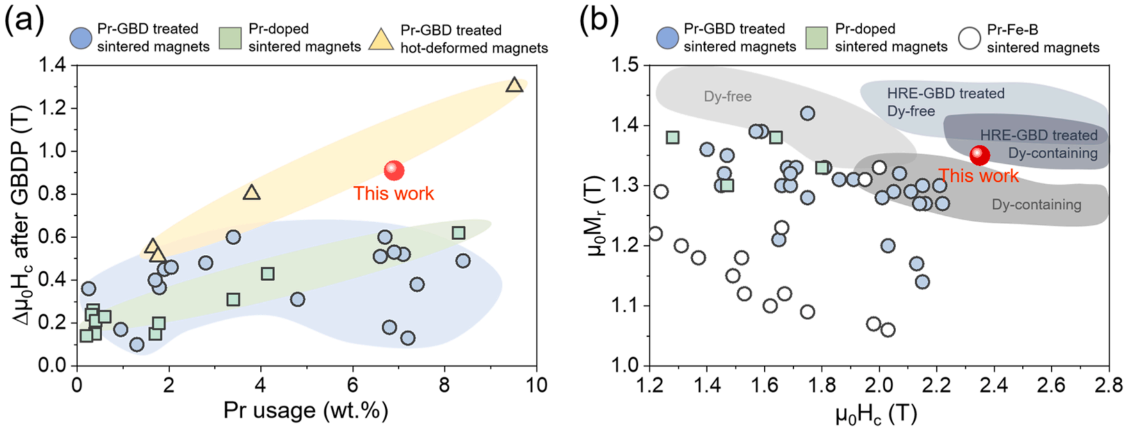

Fig. 11. (a) μ_0H_c gain by Pr-GBDP and Pr-doping as a function of Pr usage, which are reported in the literatures [21,24,25,28,29,30,35–37,66–70]. The blue circles and yellow triangles correspond to the Pr-GBD treated sintered and hot-deformed magnets, respectively, and the green squares correspond to the Pr-doped sintered magnets. (b) μ_0H_c and μ_0M_r of Pr-GBD treated (blue circles), Pr-doped (green squares), and Pr-Fe-B (white circles) sintered magnets [8,20,24,26–29,35,66,72–76]. The hard magnetic properties for commercial base magnets and HRE-GBD treated magnets are also displayed [41].

enlarged until a $\mu_0H_z = -1.84$ T, and it expanded to dozens of grain sizes under −1.85 T. The reversed domain nucleated at the interface between the shell and GBP and expanded to the core; hence, the high Pr-substitution rate shell effectively prevented the nucleation of the reversed domain owing to its high K_{u1}. The density of the magnetic Gibbs-free-energy in Fig. 10(c) proves the energy vulnerability of the TJP regions. The core was unstable than the shell, but the most unstable point was on the shell because the demagnetization field arises strongly on the TJP regions. If the Pr-concentration of the shell is increased, the energy barrier in the shell region that needs to be overcome for demagnetization under the reversed magnetic field is increased due to increase in K_{u1} of the shell, hence, the instability caused by the demagnetization field will be offset. This suggests that even if the shell is thin, a high Pr-concentration can effectively enhance the stability of the nucleation point and increase the μ_0H_c, as shown in Figs. 1(a) and 7. The positive effect of the high substitution rate of shell on the μ_0H_c offsets the negative effects of the thin shell.

Fig. 11(a) shows the μ_0H_c gain by the Pr-GBDP or Pr-doping as a function of the Pr usage, which was reported in the literature [21,24,25,28–30,35–37,66–70]. As described above, in the case of sintered magnets (blue circles), the μ_0H_c gain by the Pr-GBDP is limited to ~0.6 T, even when the Pr usage increases to ~8.5 wt.%. In the case of hot-deformed magnets, the μ_0H_c gain linearly increases from ~0.6 to ~1.3 T with increasing the Pr usage from ~2 to ~9.5 wt.%, as shown by the yellow triangles in Fig. 11(a). Such a large μ_0H_c gain by the GBDP with light rare-earth elements (Nd or Pr), which is commonly observed in hot-deformed magnets, is accompanied by a considerable reduction in the μ_0M_r as reported by Seelam et al [71]. The linear relationship between the μ_0H_c gain and Pr usage is also observed in the Pr-doped magnets (green squares), but the efficiency of Pr usage in the μ_0H_c improvement is poorer than that for the Pr-GBDP. It can be clearly seen in Fig. 11(a) that the two-step GBDP with TaF_5 and $Pr_{70}Cu_{15}Al_{10}Ga_5$ (red circle) is a promising method that can breakthrough the limit of the μ_0H_c gain of sintered magnets with the Pr-GBDP. The μ_0H_c and μ_0M_r of Pr-GBD treated (blue circles), Pr-doped (green squares), and Pr-Fe-B (white circles) sintered magnets are summarized in Fig. 11(b) [8,20,24,26–29,35,66,72–76]. The magnetic properties of commercial sintered and HRE-GBD treated magnets are also displayed [41]. The limit of μ_0H_c achievable with the Pr-GBDP is ~2.2 T, and their magnetic properties are comparable to those of commercial Dy-containing sintered magnets, as shown in Fig. 11(b). Surprisingly, by the HRE-free two-step GBDP developed in this work, the μ_0H_c limit of Pr-GBDP magnets was overcome, thereby achieving the excellent hard magnetic properties that correspond to the commercial HRE-GBD treated Dy-containing sintered magnets, as shown in Fig. 11(b).

4. Conclusions

We have successfully developed a novel CILFM-inhibited GBDP to achieve high-μ_0H_c in Nd-Fe-B sintered magnets without using HRE. In order to inhibit CILFM that inevitably occurs during the Pr-GBDP, the two-step GBDP consisting of TaF_5-GBDP (1st-GBDP) for forming the intergranular PPTs and $Pr_{70}Cu_{15}Al_{10}Ga_5$-GBDP (2nd-GBDP) for forming the high-μ_0H_a Pr-rich shell was applied to the HRE-free sintered magnets. Surprisingly, by the two-step GBDP, a large μ_0H_c gain of 0.91 T was achieved, thereby obtaining μ_0H_c of 2.35 T in the magnets without using HRE. In the magnets 1st-GBD treated with TaF_5, the hexagonal-TaB_2 PPTs with sizes of 10−30 nm are formed along the Nd-rich GBP. Due to this, CILFM occurred to form the Pr-rich shell during the 2nd-GBDP with $Pr_{70}Cu_{15}Al_{10}Ga_5$ was effectively inhibited, thereby decreasing the grain size and forming a thinner Pr-rich shell with a higher Pr-concentration compared to the one-step $Pr_{70}Cu_{15}Al_{10}Ga_5$-GBDP magnets in which the CILFM actively occurred. The micromagnetic simulation proved that the nucleation field at the interface between the 2–14–1 grain and Nd-rich phase increased when the thickness and Pr-concentration of the shell became thinner and higher, thereby increasing the μ_0H_c of the magnets. The GBD-depth of Pr also increased in the two-step GBDP magnets because the number of Pr atoms involved in the shell formation near the magnet surface decreased by the CILFM inhibition. This is another contributor for obtaining a high-μ_0H_c by the two-step GBDP. We believe that the CILFM-inhibited GBDP is a promising method that can eliminate the need for HRE in obtaining high-μ_0H_c in Nd-Fe-B sintered magnets.

CRediT authorship contribution statement

Seol-mi Lee: Writing – original draft, Methodology, Investigation, Formal analysis, Data curation. **Ganghwi Kim:** Visualization, Software, Methodology. **Ki-Suk Lee:** Visualization, Software, Methodology, Data curation. **Sumin Kim:** Visualization, Formal analysis, Data curation. **Tae-Hoon Kim:** Writing – review & editing, Visualization, Validation, Supervision, Methodology, Funding acquisition, Data curation, Conceptualization. **Sang-hyub Lee:** Validation, Resources. **Dong-Hwan Kim:** Visualization, Validation, Resources. **Wooyoung Lee:** Validation, Supervision, Methodology. **Jung-Goo Lee:** Writing – review & editing, Validation, Methodology, Investigation, Conceptualization.

Declaration of competing interest

The authors declare that they have no known competing financial interests or personal relationships that could have appeared to influence the work reported in this paper.

Acknowledgements

This research was supported by the Nano & Material Technology Development Program through the National Research Foundation of Korea (NRF) funded by Ministry of Science and ICT (RS-2023-00282096) and the Fundamental Research Program of the Korea Institute of Materials Science (PNK9960).

References

[1] O. Gutfleisch, M.A. Willard, E. Brück, C.H. Chen, S.G. Sankar, J.P. Liu, Magnetic materials and devices for the 21st century: stronger, lighter, and more energy efficient, Adv. Mater. 23 (2011) 821–842.

[2] K. Hono, H. Sepehri-Amin, Strategy for high-coercivity Nd–Fe–B magnets, Scr. Mater. 67 (2012) 530–535.

[3] S.H. Hong, Technical trends in motors of electric vehicles and changes in requirement for permanent magnets, in: Proceedings of the Symposium on Future Mobility and Permanent Magnets, Seoul, Korea, 2023.

[4] M. Sagawa, S. Hirosawa, H. Yamamoto, S. Fujimura, Y. Matsuura, Nd–Fe–B permanent magnet materials, Jpn. J. Appl. Phys. 26 (1987) 785.

[5] W.F. Li, H. Sepehri-Amin, T. Ohkubo, N. Hase, K. Hono, Distribution of Dy in high-coercivity (Nd,Dy)-Fe-B sintered magnet, Acta Mater. 59 (2011) 3061–3069.

[6] T.H. Kim, T.T. Sasaki, T. Ohkubo, Y. Takada, A. Kato, Y. Kaneko, K. Hono, Microstructure and coercivity of grain boundary diffusion processed Dy-free and Dy-containing Nd Fe B sintered magnets, Acta Mater. 172 (2019) 139–149.

[7] T.G. Woodcock, Y. Zhang, G. Hrkac, G. Ciuta, N.M. Dempsey, T. Schrefl, O. Gutfleisch, D. Givord, Understanding the microstructure and coercivity of high performance NdFeB-based magnets, Scr. Mater. 67 (2012) 536–541.

[8] H.X. Zeng, Z.W. Liu, J.S. Zhang, X.F. Liao, H.Y. Yu, Towards the diffusion source cost reduction for NdFeB grain boundary diffusion process, J. Mater. Sci. Technol. 36 (2020) 50–54.

[9] H. Nakamura, K. Hirota, M. Shimao, T. Minowa, M. Honshima, Magnetic properties of extremely small Nd-Fe-B sintered magnets, IEEE Trans. Magn. 41 (2005) 3844–3846.

[10] K. Hirota, H. Nakamura, T. Minowa, M. Honshima, Coercivity enhancement by the grain boundary diffusion process to Nd–Fe–B sintered magnets, IEEE Trans. Magn. 42 (2006) 2909–2911.

[11] H. Sepehri-Amin, T. Ohkubo, K. Hono, The mechanism of coercivity enhancement by the grain boundary diffusion process of Nd-Fe-B sintered magnets, Acta Mater. 61 (2013) 1982–1990.

[12] K. Löewe, C. Brombacher, M. Katter, O.L. Gutfleisch, Temperature-dependent Dy diffusion processes in Nd-Fe-B permanent magnets, Acta Mater. 83 (2015) 248–255.

[13] T.H. Kim, S.R. Lee, H.J. Kim, M.W. Lee, T.S. Jang, Simultaneous application of Dy–X (X= F or H) powder doping and dip-coating processes to Nd–Fe–B sintered magnets, Acta Mater. 93 (2015) 95–104.

[14] T.H. Kim, T.T. Sasaki, T. Koyama, Y. Fujikawa, M. Miwa, Y. Enokido, T. Ohkubo, K. Hono, Formation mechanism of Tb-rich shell in grain boundary diffusion processed Nd-Fe-B sintered magnets, Scr. Mater. 178 (2020) 433–437.

[15] Y.I. Lee, Y.J. Wong, H.W. Chang, W.C. Chang, Coercivity enhancement of hot-deformed NdFeB magnets by doping R80Ga20 (R = Pr, Dy, Tb) alloys, J. Magn. Magn. Mater. 478 (2019) 43–47.

[16] W. Chen, Y.L. Huang, J.M. Luo, Y.H. Hou, X.J. Ge, Y.W. Guan, Z.W. Liu, Z. C. Zhong, G.P. Wang, Microstructure and improved properties of sintered Nd-Fe-B magnets by grain boundary diffusion of non-rare earth, J. Magn. Magn. Mater. 476 (2019) 134–141.

[17] J. He, J. Cao, Z. Yu, W. Song, H. Yu, M. Hussain, Z. Liu, Grain boundary diffusion sources and their coating methods for Nd-Fe-B permanent magnets, Metals 11 (2021) 1434.

[18] M. Komuro, Y. Satsu, H. Suzuki, Increase of coercivity and composition distribution in fluoride-diffused NdFeB sintered magnets treated by fluoride solutions, IEEE Trans. Magn. 46 (2010) 3831–3833.

[19] W. Chen, J. Jin, S. Ren, B. Peng, L. Zhou, C. Wu, G. Liu, M. Yan, Unusual surface microstructural evolution of Nd–Ce–Fe–B sintered magnets by (Nd, Pr)Hx grain boundary diffusion, Mater. Charact. 190 (2022) 112073.

[20] C. Zhu, X. Liu, X. Kan, Y. Liu, L. Wang, Effect of grain boundary diffusion Pr and Cu on properties of sintered Nd-Fe-B permanent magnet, J. Supercond. Nov. Magn. 36 (2023) 1977–1982.

[21] Z. Wang, J. Zhang, J. Wang, J. Ju, R. Chen, X. Tang, W. Yin, D. Lee, A. Yan, Coercivity improvement of hot-deformed Nd-Fe-B magnets by stress-induced Pr-Cu eutectic diffusion, Acta Mater. 156 (2018) 136–145.

[22] H. Zeng, Z. Liu, W. Li, J. Zhang, L. Zhao, X. Zhong, H. Yu, B. Guo, Significantly enhancing the coercivity of NdFeB magnets by ternary Pr-Al-Cu alloys diffusion and understanding the elements diffusion behavior, J. Magn. Magn. Mater. 471 (2019) 97–104.

[23] T. Song, X. Tang, W. Yin, R. Chen, A. Yan, Coercivity enhancement of hot-pressed magnet prepared by HDDR Nd-Fe-B powders using Pr-Cu eutectic alloys diffusion, J. Magn. Magn. Mater. 471 (2019) 105–109.

[24] S. Cao, X. Bao, J. Li, H. Yu, K. Zhu, X. Gao, Improvement of microstructure and coercivity for Nd-Fe-B sintered magnets by boundary introducing low melting point alloys, J. Rare Earths 38 (2020) 395–401.

[25] Z. Wang, S. Fan, J. Zhu, B. Zheng, G. Ding, S. Guo, R. Chen, A. Yan, M. Zhang, J. Guo, Effect of PrFe alloy grain boundary diffusion on coercivity and microstructure of sintered Nd-Fe-B magnets, J. Magn. Magn. Mater. 555 (2022) 169324.

[26] Z. Jin, G. Ding, X. Fan, S. Cao, S. Fan, Z. Wang, B. Zheng, S. Guo, R. Chen, A. Yan, X. Liu, Temperature-dependent microstructure and magnetic properties evolution in the sintered Nd-Fe-B magnets with Pr-Al-Cu diffusion, J. Alloys Compd. 926 (2022) 166725.

[27] F. Li, J. Li, S.U. Ur Rehman, L. Zhang, Y. Hu, M. Yang, X. Yu, S. Zhong, T. Liang, Pr80Al20 surface-coated DyF3 modified sintered Nd-Fe-B magnets for large coercivity increment via grain boundary diffusion, J. Alloys Compd. 899 (2022) 163270.

[28] Y.J. Wong, B.S. Lin, H.W. Chang, W.C. Chang, C.H. Chiu, C.C. Mo, Enhancement of coercivity and thermal stability of Pr85Al15 doped NdFeB sintered magnets followed with grain boundary diffusion, J. Magn. Magn. Mater. 571 (2023) 170562.

[29] J. He, J. Hu, B. Zhou, H. Jia, X. Liu, Z. Zhang, L. Wen, L. Zhao, H. Yu, X. Zhong, X. Zhang, Z. Liu, Simultaneous enhancement of coercivity and electric resistivity of Nd-Fe-B magnets by Pr-Tb-Al-Cu synergistic grain boundary diffusion toward high-temperature motor rotors, J. Mater. Sci. Technol. 154 (2023) 54–64.

[30] Q. Jiang, G. Yang, C. Zhao, Q. Huang, W. Wei, H. Li, Q. Ma, Z. Zhong, The effect of PrCuGa grain boundary diffusion on the magnetic properties and microstructure of sintered Nd-La-Y-Fe-B magnet, J. Magn. Magn. Mater. 587 (2023) 171325.

[31] M. Zhao, X. Tang, W. Yin, C. Jin, J. Ju, R. Chen, A. Yan, Modification on grain boundary phase distribution in PrNd-Cu alloy diffused hot-deformed Nd-Fe-B magnets, J. Magn. Magn. Mater. 565 (2023) 170185.

[32] Z. Wei, X. Zhang, C. Zeng, Z. Yu, J. Cao, H. Yu, J. He, Z. Liu, Clarifying the dominated coercivity enhancement mechanism of grain boundary diffused Nd-Fe-B magnets by Pr-based alloys, J. Magn. Magn. Mater. 589 (2024) 171593.

[33] M. Yan, W. Chen, J. Jin, Y. Liu, H. Chen, S.P. Ringer, J. Xu, Y. Hou, M. Yue, X. Liu, Merits of Pr80Ga20 grain boundary diffusion process towards high coercivity−remanence synergy of Nd−La−Ce−Fe−B sintered magnet, Acta Mater. 231 (2022) 117873.

[34] J. Jin, W. Chen, M. Bu, L. Zhou, B. Peng, W. Li, M. Yan, Comparative study of Pr/PrFe/PrAl grain boundary diffusion processed Nd–Ce–Fe–B sintered magnets with high Ce substitution: evolutionary microstructure and magnetic responses, Acta Mater. 257 (2023) 119175.

[35] L. Jin, Z.H. Jin, J.H. Zhu, G.F. Ding, B. Zheng, S. Guo, R.J. Chen, A.R. Yan, X.C. Liu, Coercivity and microstructure of sintered Nd–Fe–B magnets diffused with Pr−Co, Pr−Al, and Pr−Co−Al alloys, Chin. Phys. B 30 (2021) 027503.

[36] H. Peng, D. Yu, X. Bai, X. Lin, Y. Mao, Z. Wang, Y. Luo, Effects of grain boundary diffusion of PrCu alloy on microstructure and coercivity of hot deformed (Nd, Ce)-Fe-B magnets, J. Rare Earths 39 (2021) 986–992.

[37] B. Chen, X. Tang, W. Yin, T. Song, J. Ju, A. Yan, R. Chen, F. Wang, Coercivity enhancement of hot-deformed (Ce, Nd, Pr)-Fe-B magnets by grain boundary diffusion of Pr-Cu alloy, J. Magn. Magn. Mater 497 (2020) 166002.

[38] H. Sepehri-Amin, L. Liu, T. Ohkubo, M. Yano, T. Shoji, A. Kato, T. Schrefl, K. Hono, Microstructure and temperature dependent of coercivity of hot-deformed Nd–Fe–B magnets diffusion processed with Pr−Cu alloy, Acta Mater. 99 (2015) 297–306.

[39] S. Kim, D.S. Ko, H.S. Lee, D. Kim, J.W. Roh, W. Lee, Enhancing the coercivity of Nd-Fe-B sintered magnets by consecutive heat treatment-induced formation of Tb-diffused microstructures, J. Alloy. Compd. 780 (2019) 574–580.

[40] Z. Wang, T.T. Sasaki, Y. Une, T. Ohkubo, K. Hono, Substantial coercivity enhancement in Dy-free Nd-Fe-B sintered magnet by Dy grain boundary diffusion, Acta Mater. 248 (2023) 118774.

[41] Catalogue of Shin-Etsu Chemical Co., Ltd. (2024) http://www.shinetsu-rare-earth-magnet.jp/e/products/data_nd.html.

[42] T.T. Sasaki, T. Ohkubo, Y. Takada, T. Sato, A. Kato, Y. Kaneko, K. Hono, Formation of non-ferromagnetic grain boundary phase in a Ga-doped Nd-rich Nd-Fe-B sintered magnet, Scr. Mater. 113 (2016) 218–221.

[43] T.H. Kim, S.R. Lee, K.H. Bae, H.J. Kim, M.W. Lee, T.S. Jang, Effects of Al/Cu co-doping on crystal structure and chemical composition of Nd-rich phases in Nd-Fe-B sintered magnet, Acta Mater. 133 (2017) 200–207.

[44] T.H. Kim, S.R. Lee, M.W. Lee, T.S. Jang, J.W. Kim, Y.D. Kim, H.J. Kim, Dependence of magnetic, phase-transformation and microstructural characteristics on the Cu content of Nd–Fe–B sintered magnet, Acta Mater. 66 (2014) 12–21.

[45] H.K. Rang, S. Hackney, D.N. Yoon, Migration of liquid film and grain boundary in Mo-Ni induced by W diffusion, Acta Metall. 36 (1988) 695–699.

[46] D.N. Yoon, Chemically induced interface migration in solids, Annu. Rev. Mater. Sci. 19 (1989) 43–58.

[47] T. Oikawa, H. Yokota, T. Ohkubo, K. Hono, Large-scale micromagnetic simulation of Nd-Fe-B sintered magnets with Dy-rich shell structures, AIP Adv. 6 (2016) 056006.

[48] A. Yan, X. Song, X. Wang, Effect of minor intergranular additives on microstructure and magnetic properties of NdFeB based magnets, J. Magn. Magn. Mater. 169 (1997) 193–198.

[49] T.S. Chin, C.H. Lin, Y.H. Huang, J.M. Yau, S.J. Heh, F.D. King, Enhanced thermal stability of sintered (Nd, Dy)(Fe, Co) B magnets by the addition of Ta or Ti, IEEE Trans. Magn. 29 (1993) 2788–2790.

[50] X. Bao, X. Gao, J. Zhu, S. Zhou, Effect of zirconium content on exchange coupling and magnetization reversal of nanocrystalline Nd12.3Fe81.7–xZrxB6 alloy, J. Rare Earths 29 (2011) 939–942.

[51] K.H. Bae, S.R. Lee, H.J. Kim, M.W. Lee, T.S. Jang, Effect of WS2/Al co-doping on microstructural and magnetic properties of Nd-Fe-B sintered magnets, J. Alloy. Compd. 673 (2016) 321–326.

[52] Z. Qiaoying, C. Renjie, L. Zhuang, G. Shuai, Y. Aru, L. Dong, Effect of refractory metal substitution on magnetic property and corrosion behavior of sintered NdFeB magnets, Rare Met. Mater. Eng. 44 (2015) 2376–2380.

[53] M. Itakura, K. Sugiyama, H. Akamine, M. Nishida, M. Nakamura, T. Mizoguchi, T. Iriyama, Suppression mechanism of abnormal grain growth by Zr addition in pressless processed Nd-Fe-B sintered magnets, J. Alloy. Compd. 887 (2021) 161244.

[54] G.N. Papatheodorou, S. Boghosian, Glass formation and phase transitions of NbF5 and TaF5 from 77 to 600 K, in: Proceedings of the ECS 294, 2004, pp. 2004–2024.

[55] R.F. Krause Jr, T.B. Douglas, The melting temperature, vapor density, and vapor pressure of molybdenum pentafluoride, J. Chem. Thermodyn. 9 (1977) 1149–1163.

[56] L.D. Landau, E.M. Lifshitz, Theory of the dispersion of magnetic permeability in ferromagnetic bodies, Physiol. Z. Sowietunion 8 (1935) 153–169.

[57] T.L. Gilbert, Lagrangian formulation of the gyromagnetic equation of the magnetization field, Physiol. Rev. 100 (1955) 1243.

[58] A. Vansteenkiste, J. Leliaert, M. Dvornik, M. Helsen, F. Garcia-Sanchez, B.V. Van Waeyenberge, The design and verification of MuMax3, AIP Adv. 4 (2014) 107133.

[59] S. Hirosawa, Y. Matsuura, H. Yamamoto, S. Fujimura, M. Sagawa, H. Yamauchi, Magnetization and magnetic anisotropy of R2Fe14B measured on single crystals, J. Appl. Phys. 59 (1986) 873–879.

[60] H. Sepehri-Amin, T. Ohkubo, S. Nagashima, M. Yano, T. Shoji, A. Kato, T. Schrefl, K. Hono, High-coercivity ultrafine-grained anisotropic Nd-Fe-B magnets processed by hot deformation and the Nd-Cu grain boundary diffusion process, Acta Mater. 61 (2013) 6622–6634.

[61] J. Li, L. Liu, H. Sepehri-Amin, X. Tang, T. Ohkubo, N. Sakuma, T. Shoji, A. Kato, T. Schrefl, K. Hono, Coercivity and its thermal stability of Nd-Fe-B hot-deformed magnets enhanced by the eutectic grain boundary diffusion process, Acta Mater. 161 (2018) 171–181.

[62] T.H. Kim, S.R. Lee, S.J. Yun, S.H. Lim, H.J. Kim, M.W. Lee, T.S. Jang, Anisotropic diffusion mechanism in grain boundary diffusion processed Nd-Fe-B sintered magnet, Acta Mater. 112 (2016) 59–66.

[63] G.W. Hu, L.C. Zeng, H. Du, Q. Wang, Z.T. Fan, X.W. Liu, Combined effects of solute drag and Zener pinning on grain growth of a NiCoCr medium-entropy alloy, Intermetallics 136 (2021) 107271.

[64] H. Sepehri-Amin, T. Ohkubo, T. Shima, K. Hono, Grain boundary and interface chemistry of an Nd–Fe–B-based sintered magnet, Acta Mater. 60 (2012) 819–830.

[65] T.T. Sasaki, T. Ohkubo, K. Hono, Structure and chemical compositions of the grain boundary phase in Nd-Fe-B sintered magnets, Acta Mater. 115 (2016) 269–277.

[66] M. Tang, X. Bao, Y. Zhou, K. Lu, J. Li, X. Gao, Microstructure and annealing effects of NdFeB sintered magnets with Pr-Cu boundary addition, J. Magn. Magn. Mater. 505 (2020) 166749.

[67] J. Li, X. Huang, L. Zeng, B. Ouyang, X. Yu, M. Yang, B. Yang, R.S. Rawat, Z. Zhong, Tuning magnetic properties, thermal stability and microstructure of NdFeB magnets with diffusing Pr-Zn films, J. Mater. Sci. Technol. 41 (2020) 81–87.

[68] J. Jin, M. Yan, W. Chen, W. Zhang, Z. Zhang, L. Zhao, G. Bai, J.M. Greneche, Grain boundary engineering towards high-figure-of-merit Nd-Ce-Fe-B sintered magnets: synergetic effects of (Nd, Pr)Hx and Cu co-dopants, Acta Mater. 204 (2021) 116529.

[69] T. Ma, B. Wu, Y. Zhang, J. Jin, K. Wu, S. Tao, W. Xia, M. Yan, Enhanced coercivity of Nd-Ce-Fe-B sintered magnets by adding (Nd, Pr)-H powders, J. Alloy. Compd. 721 (2017) 1–7.

[70] S. Cao, S. Zheng, Z. Jia, Z. Xiong, G. Ding, X. Fan, S. Guo, B. Zheng, R. Chen, C. Yan, A. Yan, Coercivity enhancement of NdCeFeB magnet by two-step grain boundary diffusion with Pr70Cu10Al15Ga5 and DyHx, J. Alloy. Compd. 976 (2024) 173006.

[71] U.M.R. Seelam, L. Liu, T. Akiya, H. Sepehri-Amin, T. Ohkubo, N. Sakuma, M. Yano, A. Kato, K. Hono, Coercivity of the Nd–Fe–B hot-deformed magnets diffusion-processed with low melting temperature glass forming alloys, J. Magn. Magn. Mater. 412 (2016) 234–242.

[72] Z. Wang, S. Fan, J. Zhu, B. Zheng, G. Ding, S. Guo, R. Chen, A. Yan, M. Zhang, J. Guo, B. Zhang, Effect of PrFe alloy grain boundary diffusion on coercivity and microstructure of sintered Nd-Fe-B magnets, J. Magn. Magn. Mater. 555 (2022) 169324.

[73] R.N. Faria, X.J. Yin, J.S. Abell, I.R. Harris, Microstructural and magnetic studies of Pr-Fe-B-Cu HD sintered magnets, J. Magn. Magn. Mater. 129 (1994) 263–270.

[74] R.N. Faria, The influence of zirconium addition and process parameters on the magnetic properties of Pr-Fe-B sintered magnets, J. Magn. Magn. Mater. 238 (2022) 56–64.

[75] R.N. Faria, A.R.M. Castro, N.B. Lima, Relation between grain alignment and magnetic properties of Pr-Fe-B sintered magnets, J. Magn. Magn. Mater. 238 (2002) 38–46.

[76] H. Chen, W. Liu, T. Yang, Z. Guo, X. Xu, Y. Li, H. Zhang, M. Yue, Realization of high-performance HRE-free Pr-Fe-B sintered magnet through microstructure regulation, J. Magn. Magn. Mater. 563 (2022) 169913.